# Computationally Guided Discovery of Mixed Mn/Ni Perovskites for Solar Thermochemical Hydrogen Production at High H<sub>2</sub> Conversion

Ryan J. Morelock<sup>‡,1</sup>, Justin T. Tran<sup>‡,1</sup>, Zachary J. L. Bare<sup>1</sup>, Jamie A. Trindell<sup>2</sup>, Anthony H. McDaniel<sup>2</sup>, Alan W. Weimer<sup>1</sup> and Charles B. Musgrave<sup>\*,1,3,4</sup>

<sup>1</sup>Department of Chemical and Biological Engineering, University of Colorado Boulder, Boulder, CO 80309, USA

<sup>2</sup>Sandia National Laboratories, Livermore, CA 94550, USA

<sup>3</sup>Renewable and Sustainable Energy Institute, University of Colorado Boulder, Boulder, CO 80309, USA

<sup>4</sup>Materials Science and Engineering Program, University of Colorado Boulder, Boulder, CO 80309, USA

Keywords: density functional theory, perovskite, concentrated solar energy, thermochemical water splitting, hydrogen

#### Abstract

We computationally modeled the electronic and oxygen vacancy properties of the perovskite oxides LaMn<sub>0.5</sub>Ni<sub>0.5</sub>O<sub>3</sub> (L2MN), Gd<sub>0.5</sub>La<sub>0.5</sub>Mn<sub>0.5</sub>Ni<sub>0.5</sub>O<sub>3</sub> (GLMN) and GdMn<sub>0.5</sub>Ni<sub>0.5</sub>O<sub>3</sub> (G2MN), which were identified as candidate redox mediators for solar thermochemical hydrogen (STCH) production following a high-throughput computational screening of AA'BB'O<sub>6</sub> compositions that are likely to form as perovskites and split water. Density functional theory predicts similar electronic properties and oxygen vacancy thermodynamics for the previously-

synthesized perovskites L2MN and G2MN, and the previously unknown perovskite GLMN, but slower oxygen vacancy diffusion kinetics as Gd is substituted for La. At a thermal reduction temperature of 1350 °C and a water splitting temperature of 850 °C, the L2MN and GLMN perovskites produced ~65 μmol g<sup>-1</sup> of hydrogen per cycle with limited phase degradation over three redox cycles at 40 mol% steam, while the G2MN perovskite was inactive for STCH. When re-oxidized by exposure to a gas flow with a H<sub>2</sub>O:H<sub>2</sub> molar ratio of 1333:1, which represents the operating conditions of industrial reactors where the thermodynamic driving force of water splitting is lowered by *orders of magnitude* relative to 40 mol% steam, the L2MN and GLMN perovskites each produced ~35 μmol g<sup>-1</sup> of hydrogen per cycle.

### Introduction

Solar thermochemical hydrogen production is a promising approach for generating renewable hydrogen using only steam and the thermal energy of sunlight as inputs.  $^{1,2}$  Solar thermochemical hydrogen (STCH) is typically produced using a two-step reduction/oxidation cycle,  $^{3,4}$  during which a metal oxide redox mediator first undergoes significant thermal reduction whereby the mediator spontaneously evolves  $O_2$  from its crystal lattice or through decomposition under inert conditions at high reduction temperatures of  $1100 \text{ °C} \leq T_{TR} \leq 2000 \text{ °C}$ . The reduced material is subsequently cycled to lower water splitting temperatures of  $850 \text{ °C} \leq T_{WS} \leq 1100 \text{ °C}$  and exposed to steam, generating hydrogen gas and re-oxidizing the redox mediator. Industrial scale two-step STCH processes are highly desirable, as they utilize the entire solar spectrum and therefore have the potential to achieve higher theoretical efficiencies than other solar hydrogen production alternatives. However, the efficiencies achieved by STCH systems depend on operating conditions, which are dictated by the water-splitting activities of their redox mediators.

A primary goal of the STCH community is to identify novel redox materials that mediate STCH production processes with grid-scale economics.<sup>6</sup>

Currently, the STCH community is focused on nonstoichiometric oxides because their redox cycles are free from the problematic solid-vapor or solid-solid phase transitions that have hindered the development of fully stoichiometric metal oxide cycles. As such, many nonstoichiometric oxides have been explored for their STCH behavior as redox mediators.<sup>7–10</sup> These include doped  $^{11,12}$  and undoped herevnite spinels (Fe<sub>x</sub>M<sub>1-x</sub>Al<sub>2</sub>O<sub>4</sub>, M = Co, Mg, etc.),  $^{13,14}$  as well as complex perovskite oxides (A<sub>x</sub>A'<sub>1-x</sub>B<sub>y</sub>B'<sub>1-y</sub>O<sub>3</sub> compositions) such as BaCe<sub>0.25</sub>Mn<sub>0.75</sub>O<sub>3</sub>  $(BCM)^{15} \quad and \quad Sr_{0.4}La_{0.6}Mn_{0.4}Al_{0.6}O_3 \quad (SLMA).^{10,16,17} \quad Perovskite \quad oxides \quad are \quad a \quad particularly \quad are the sum of t$ compelling materials space for STCH applications due to their highly-tunable properties <sup>18</sup> and the vast number of compositions that can be stabilized in the perovskite structure. 19 The sheer size of the perovskite oxide composition space presents a considerable challenge, however, as experimental synthesis and characterization alone cannot feasibly evaluate the STCH activity of even a moderate fraction of all possible perovskite combinations. For this reason, several previous investigations have first modeled perovskite oxides to predict their STCH activity using highthroughput computational frameworks prior to experimental examination.<sup>20,21</sup> Such computational investigations provide insight into STCH-relevant properties in an attempt to reduce the number of experiments necessary to identify candidate materials, and have identified several STCH-active perovskite redox mediators.<sup>22–24</sup>

In the present work, we investigate the perovskite oxides LaMn<sub>0.5</sub>Ni<sub>0.5</sub>O<sub>3</sub> (L2MN), Gd<sub>0.5</sub>La<sub>0.5</sub>Mn<sub>0.5</sub>Ni<sub>0.5</sub>O<sub>3</sub> (GLMN) and GdMn<sub>0.5</sub>Ni<sub>0.5</sub>O<sub>3</sub> (G2MN) for STCH. These perovskites were identified from high-throughput computational investigations of theoretical Gd-containing and Mn-containing perovskite compositions for their perovskite synthesizability and STCH

activities.<sup>25</sup> The L2MN and G2MN perovskites have been previously synthesized,<sup>26</sup> but to our knowledge, not investigated for STCH activity. The GLMN perovskite has not been previously synthesized or reported for STCH. We characterized the electronic properties and oxygen vacancy thermodynamics of L2MN, GLMN and G2MN using the strongly constrained and appropriately normed<sup>27</sup> (SCAN) density functional theory (DFT) meta-GGA functional and show that these properties are very similar for all three perovskites. We next characterized the oxygen vacancy kinetics of these materials and show that the barriers to bulk oxygen diffusion are highest in G2MN. The similarities in DFT-predicted thermodynamic properties justify the similar measured hydrogen capacities of L2MN and GLMN under pure steam conversion conditions, i.e., where the redox mediators are mostly re-oxidized, while G2MN's high diffusion barrier justifies its STCH inactivity at these conditions. We also evaluated L2MN and GLMN at a steam-to-hydrogen molar ratio of 1333:1 (0.1% steam conversion conditions), which represents realistic reactor conditions at which generated STCH hydrogen is present in steam. Hydrogen in steam substantially reduces the chemical potential of oxygen, which shifts water-splitting thermodynamics to be much less favorable. As a result, few known redox mediators have demonstrated STCH activities at these conditions. However, we observed similar high conversion STCH activity in the L2MN and GLMN perovskites, which encourages further optimization of mixed Mn/Ni perovskite oxides for STCH applications.

### Results

### I. Computational Modeling of L2MN, GLMN and G2MN

A. Identification of STCH Candidate Perovskite Oxides L2MN, GLMN and G2MN

Bare et al.<sup>25</sup> reported L2MN, GLMN and G2MN as candidate STCH redox mediators following their high-throughput compositional screening investigations of Gd-containing and Mn-

containing multinary compositions (GdA'BB'O<sub>6</sub>, GdA'B<sub>2</sub>O<sub>6</sub>, and Gd<sub>2</sub>BB'O<sub>6</sub>, and AA'MnB'O<sub>6</sub>, AA'Mn<sub>2</sub>O<sub>6</sub>, and A<sub>2</sub>MnB'O<sub>6</sub>) that were predicted to be synthesizable as perovskites. The highthroughput computational framework used is described in Ref. 24, and its results for L2MN, GLMN and G2MN are restated in Section I of the SI, but is briefly discussed here. In that work we showed that the machine-learned tolerance factor  $\tau$  derived by Bartel et al.<sup>28</sup> predicts that L2MN, GLMN and G2MN are synthesizable as perovskites. Furthermore, DFT-predicted L2MN, GLMN and G2MN perovskite stabilities were reported as decomposition enthalpies<sup>29</sup> ( $\Delta H_d$ ) computed relative to competing phases tabulated in the Materials Project (MP) database. Bare et al.25 calculated all DFT energies and electronic properties using the PBE GGA+U functional to ensure compatibility with the MP. The  $\Delta H_d$ s predict that all three perovskites are on or within 60 meV atom<sup>-1</sup> of the convex hull, reinforcing that the L2MN, GLMN and G2MN compositions can be stabilized as perovskites. Bare et al.<sup>25</sup> also showed that all three perovskites exhibit non-zero band gaps  $(E_g)$ , suggesting favorable electronic properties for STCH that are discussed in more detail in the following section. Finally, L2MN, GLMN and G2MN possess mean oxygen vacancy formation enthalpies,  $\Delta \overline{H}_{Ovac}$ , within the STCH active range defined by Bare et al.,<sup>25</sup> which identified these compositions as STCH candidate perovskite oxide redox mediators. In the present work, we computationally characterized the L2MN, GLMN and G2MN perovskite oxides using the SCAN meta-GGA functional to accurately capture the STCH relevant properties of these candidate redox mediators.

### B. DFT Structures and Electronic Properties of Bulk L2MN, GLMN and G2MN

The initial L2MN, GLMN and G2MN perovskite structures used as inputs for DFT optimization were generated in the *Pnma* space group with the a-b+a- perovskite Glazer tilt<sup>30</sup> using the Structure Prediction and Diagnostic Software (SPuDS) program,<sup>31</sup> consistent with the

procedure reported by Bare et al.<sup>25</sup> L2MN, GLMN and G2MN structures were generated with rock salt B-site ordering, whereas the Ewald sum over the two Gd and two La sites was minimized for GLMN, resulting in rock salt A-site ordering. Because the SPuDS program enforces symmetry constraints on the perovskite structure A-site positions and BO<sub>6</sub> octahedra during structure generation --- and these unrealistically constrained symmetries can persist as artifacts during DFT optimization --- all sites were rattled to break site symmetries prior to DFT optimization. The positions, cell shapes and cell volumes of bulk L2MN, GLMN and G2MN were optimized such that the forces on all ions converged to less than 0.02 eV/atom, consistent with the Materials Project SCAN relaxation set. As discussed in Section II of the SI, the oxidation states of Gd, La, Mn and Ni are confirmed by DFT to be +3, +3, +4 and +2, respectively, in all three materials. The DFT optimized bulk structures of L2MN, GLMN and G2MN are displayed in Figure 1.

Figure 1 shows that, as the fraction of Gd increases relative to La, the unit cell volume generally decreases, and the length of the *b* lattice vector increases relative to that of the *c* lattice vector. This is accompanied by an increase in corner-sharing BO<sub>6</sub> octahedral tilting magnitude(s) as characterized by the Robocrystallographer python package,[REF] with tilt angles that range from 19-22° for L2MN, 24-29° for GLMN, and 31-32° for G2MN. Additionally, the equatorial B-O-B bond distances lengthen with increasing Gd content relative to axial B-O-B bond distances, which are attributed to Jahn-Teller type distortions frequently observed for NiO<sub>6</sub> and MnO<sub>6</sub> octahedra.<sup>32</sup> Averaged over the unique NiO<sub>6</sub> and MnO<sub>6</sub> octahedra in each 20-atom perovskite representation (two BO<sub>6</sub> per Ni and Mn in each structure), the equatorial-to-axial B-O-B bond length ratios of NiO<sub>6</sub> and MnO<sub>6</sub> octahedra are 1.001:1 and 1.001:1 in L2MN, and 1.020:1 and 1.010:1 in G2MN. This results in G2MN octahedra that are axially compressed. In GLMN, the equatorial-to-axial B-O-B bond length ratios of NiO<sub>6</sub> and MnO<sub>6</sub> octahedra are 1.006:1 and 1.003:1,

and its BO<sub>6</sub> octahedra are therefore partially compressed relative to L2MN. As characterized by differences in B-O-B bond distances between NiO<sub>6</sub> and MnO<sub>6</sub> octahedra *in the same structure*, GLMN octahedra are generally more distorted than L2MN and G2MN octahedra. Whereas B-O-B distances typically vary by < 0.001 Å in G2MN and L2MN compositions --- for example, the axial B-O-B are 4.044 Å and 4.044 Å for the two unique NiO<sub>6</sub> octahedra of L2MN --- these distances can vary by > 0.03 Å in GLMN, as shown by the NiO<sub>6</sub> octahedra of GLMN with axial B-O-B of 4.030 Å and 4.070 Å. These variations between B-O-B distances in GLMN arise to accommodate the different A-site elements, i.e., La and Gd, present in the GLMN perovskite lattice.

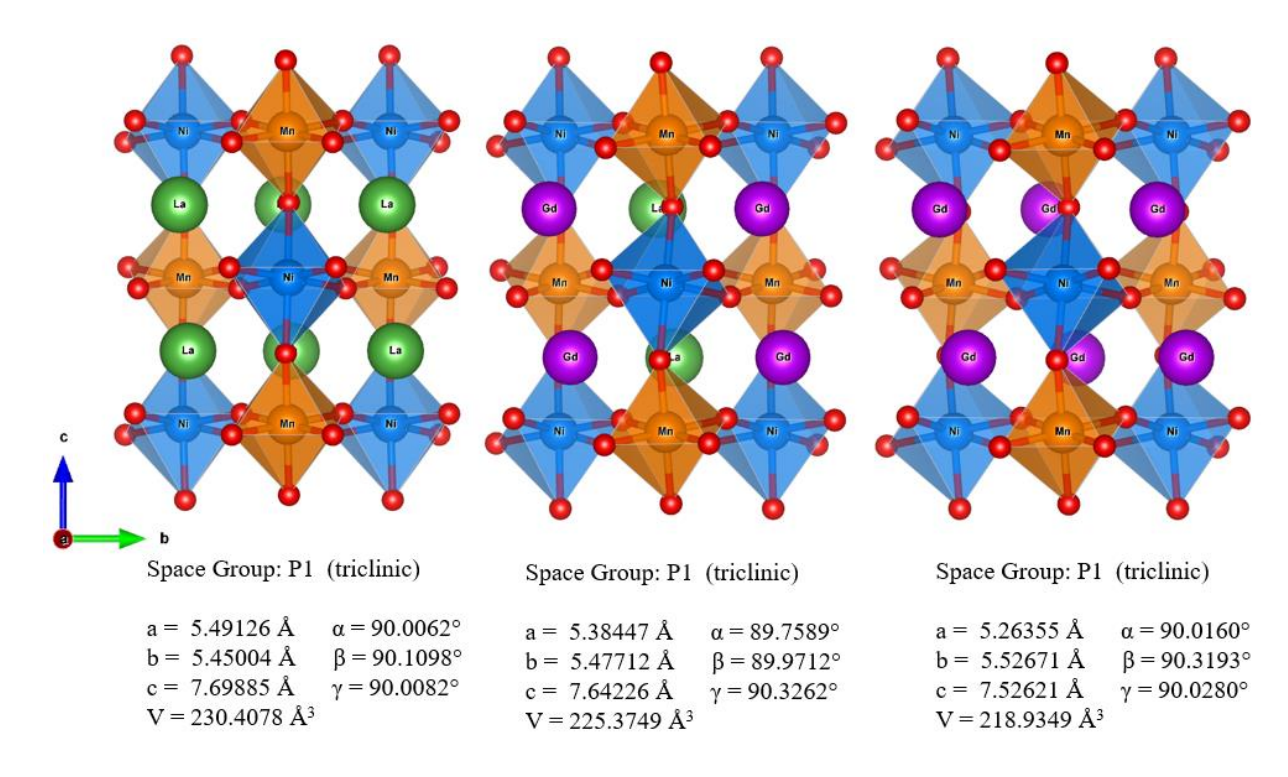


**Figure 1**. DFT-optimized perovskite structures of L2MN, GLMN and G2MN (from left to right) using the SCAN functional (see SI for PBE optimized structures). a, b and c lattice directions are shown for reference. All structures optimized to the triclinic crystal system with space group P1. As the proportion of Gd increases relative to La, the DFT predicted unit cell volumes decrease and the b/c lattice vector ratio increases, corresponding with an increase in equatorial B-O-B bond lengths relative to axial B-O-B lengths for the BO<sub>6</sub> octahedra.

Furthermore, we evaluated the band gaps,  $E_g$ , and density of states (DOS) effective masses,  $m_e^*$ , of the DFT optimized bulk perovskite phases. As described by Lany,<sup>33</sup> the multiplicity of electronic states at the conduction band minimum (CBM) is characterized by the DOS effective mass,  $m_e^*$ . Large  $m_e^*$  can contribute positive, solid-state electronic entropy of thermal reduction,  $\Delta S_{TR,elec}$ ,<sup>33</sup> which decreases the free energy of reduction,  $\Delta G_{TR}$ , especially at high reduction temperatures. Decreased  $\Delta G_{TR}$  at thermal reduction temperatures increases the concentration of oxygen vacancies formed, thereby increasing STCH production capacity and benefitting overall STCH performance.<sup>34</sup> To preferentially screen for perovskite compositions where  $m_e^*$  might contribute significantly to  $\Delta S_{TR,elec}$ , Bare et al.<sup>25</sup> did not consider any metallic perovskites, i.e., those with  $E_g = 0$  and therefore  $m_e^* = 0$ . We characterized the  $E_g$ s and  $m_e^*$ s of L2MN, GLMN and G2MN --- which were predicted by Bare et al.<sup>25</sup> to be semiconductors --- and report their element-projected DOS (pDOS) plots in **Figure 2** below, where the pDOSs are colored based upon the elements contributing electronic states.

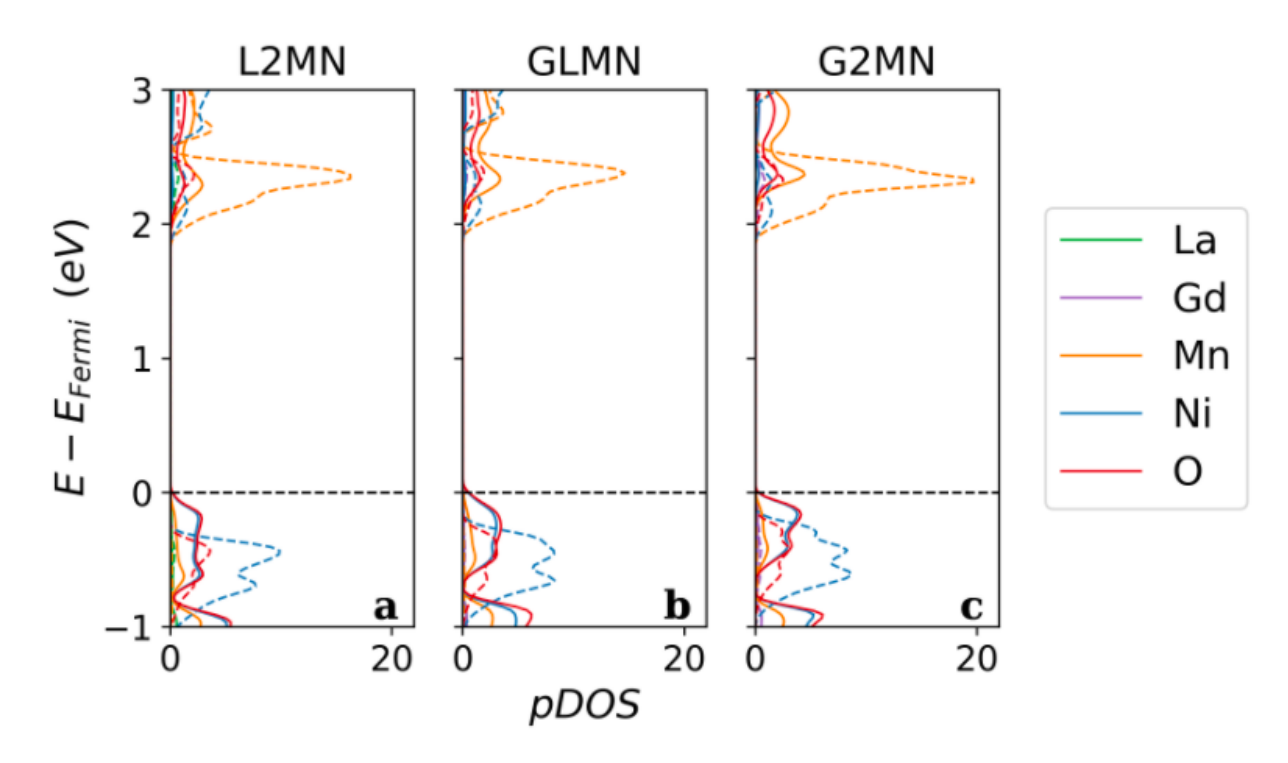


**Figure 2**. Element-projected density of states (pDOS) plots for L2MN, GLMN and G2MN. Electronic states with spin-up magnetism are indicated by the solid lines, whereas electronic states with spin-down magnetism are indicated by the dashed lines. L2MN, GLMN and G2MN exhibit  $E_g$ s of 1.88 eV, 1.92 eV, and 1.93 eV, respectively, and  $m_e^*$ s of 4.44, 4.43 and 5.21, respectively. La, Gd, Mn, Ni and O electronic states are designated by the colors green, purple, orange, blue and red, respectively.

Our results show that all three compositions are semiconductors, in agreement with the results reported by Bare et al.<sup>25</sup> For all three compositions, the valence band maximum (VBM) is dominated by O and Ni electronic states and the CBM is dominated by Mn electronic states with some Ni character, consistent with previous computational investigations of complex perovskite oxides that showed that the electronic states of perovskite B and X-sites typically dictate  $E_g$ .<sup>35</sup> The band gaps and  $m_e^*$ s of L2MN, GLMN and G2MN are markedly similar, with computed  $E_g$ s of 1.88 eV, 1.92 eV, and 1.93 eV, and computed  $m_e^*$ s of 4.44, 4.43 and 5.21, respectively. As shown in Section III of the SI, all compositions possess a large number of similar-energy lanthanide

electronic states between 4-6 eV above the Fermi level. These states are energetically inaccessible at practical STCH reduction temperatures,  $T_{TR} < 1500^{\circ}\text{C}$ , and therefore do not contribute to the  $m_e^*$ . Despite this, G2MN has a larger  $m_e^*$  than L2MN and GLMN, consistent with the results reported by Bare et al. that showed that the substitution of Gd<sup>3+</sup> for La<sup>3+</sup> in ABO<sub>3</sub> perovskite oxides generally increases  $m_e^*$ . However, for the La-Gd-Mn-Ni-O systems investigated herein this increase in  $m_e^*$  is caused by the *slight increase* in Mn electronic state density near the CBM when Gd is fully substituted for La, rather than a large density of unoccupied Gd electronic states near the CBM. Although DFT predicts small changes in  $m_e^*$ s between both L2MN and GLMN, and G2MN, the similarities between their electronic properties suggest similar solid-state  $\Delta S_{TR,elec}$  contributions to the Gibbs free energies of reduction,  $\Delta G_{TR}$ s, in these materials.

### C. DFT Oxygen Vacancy Defect Properties of L2MN, GLMN and G2MN

Known STCH perovskite redox mediators --- including Sr<sub>0.6</sub>La<sub>0.4</sub>Mn<sub>0.6</sub>Al<sub>0.4</sub>O<sub>3</sub> (SLMA)<sup>16</sup> and BaCe<sub>0.25</sub>Mn<sub>0.75</sub>O<sub>3</sub> (BCM)<sup>15</sup> --- are reduced by off-stoichiometric mechanisms,<sup>36</sup> whereby oxygen vacancies form at STCH thermal reduction temperatures while the perovskite structure is preserved. This mechanism enables these perovskite redox mediators to maintain the perovskite phase for many redox cycles, resulting in their near-constant STCH production and their overall durability. For the present investigation, we evaluated the DFT oxygen vacancy formation enthalpies,  $\Delta H_{Ovac}$ , of L2MN, GLMN and G2MN using Equation (1), which assumes these materials also operate through the off-stoichiometric reduction mechanism:

$$\Delta H_{Ovac} = E_{tot}^{defect} - E_{tot}^{host} + \mu_O, \tag{1}$$

where  $E_{tot}^{host}$  is the DFT total energy of the bulk perovskite oxide,  $E_{tot}^{defect}$  is the DFT total energy of the reduced perovskite oxide, and  $\mu_0$  is the DFT-computed chemical potential of oxygen. We calculated  $E_{tot}^{defect}$  for all unique oxygen vacancy sites present in the 20-atom bulk perovskite

oxides, as determined using pymatgen's SpacegroupAnalyzer module, and computed  $\mu_O$  as the energy per atom of a single O<sub>2</sub> molecule isolated in a 10 Å x 10 Å x 10 Å unit cell. As shown in Section IV of the SI, the choice of reference  $\mu_O$  changes the absolute predictions of  $\Delta H_{Ovac}$ , but does not change the relative predictions of  $\Delta H_{Ovac}$  between redox mediator candidates.

The 0 K  $\Delta H_{Ovac}$ s computed using DFT are often used to estimate the thermal reduction enthalpies of STCH materials,  $\Delta H_{TR}$ s, which along with  $\Delta S_{TR}$  define  $\Delta G_{TR}$ . Viable STCH redox mediators should have  $\Delta H_{TR}$  greater than the standard state formation enthalpy of steam,  $\Delta H_{H_2O(q)}$  $\approx 2.5$  eV atom<sup>-1</sup>, as redox mediators with  $\Delta H_{H_2O(g)} < 2.5$  eV atom<sup>-1</sup> may still split water but typically incur unfavorable energetic penalties during STCH cycling. Rather than compare the DFT-computed  $\Delta H_{ovac}$  of L2MN, GLMN and G2MN to the experimental  $\Delta H_{H_2O(g)}$ , in the present work we compared  $\Delta H_{ovac}$ s to the DFT-computed  $\Delta H_{ovac}$  of the gold-standard STCH perovskite redox mediator, CeO<sub>2</sub> (ceria). At reduction temperatures between 1500°C  $\leq T_{TR} \leq$  2000°C, CeO<sub>2</sub> exhibits exceptional STCH hydrogen production<sup>37</sup> and functions by an off-stoichiometric reduction mechanism<sup>38</sup> similar to that reported in STCH active perovskite oxides. However, the large  $\Delta H_{TR}$  of CeO<sub>2</sub> leads to insufficient hydrogen production at  $T_{TR} = 1350$ °C, and even at  $T_{TR} \le$ 1500°C. 15 To avoid the complexities of engineering ultra-high temperature industrial STCH reactors, a thermal reduction temperature  $T_{TR} < 1500$  °C is desired. Commercially viable STCH perovskite oxide candidates should therefore have computationally predicted  $\Delta H_{Ovac}$  less than that of ceria. The  $\Delta H_{Ovac}$  calculation results for L2MN, GLMN and G2MN, as well as the  $\Delta H_{Ovac}$  of CeO<sub>2</sub>, are shown in Figure 3.

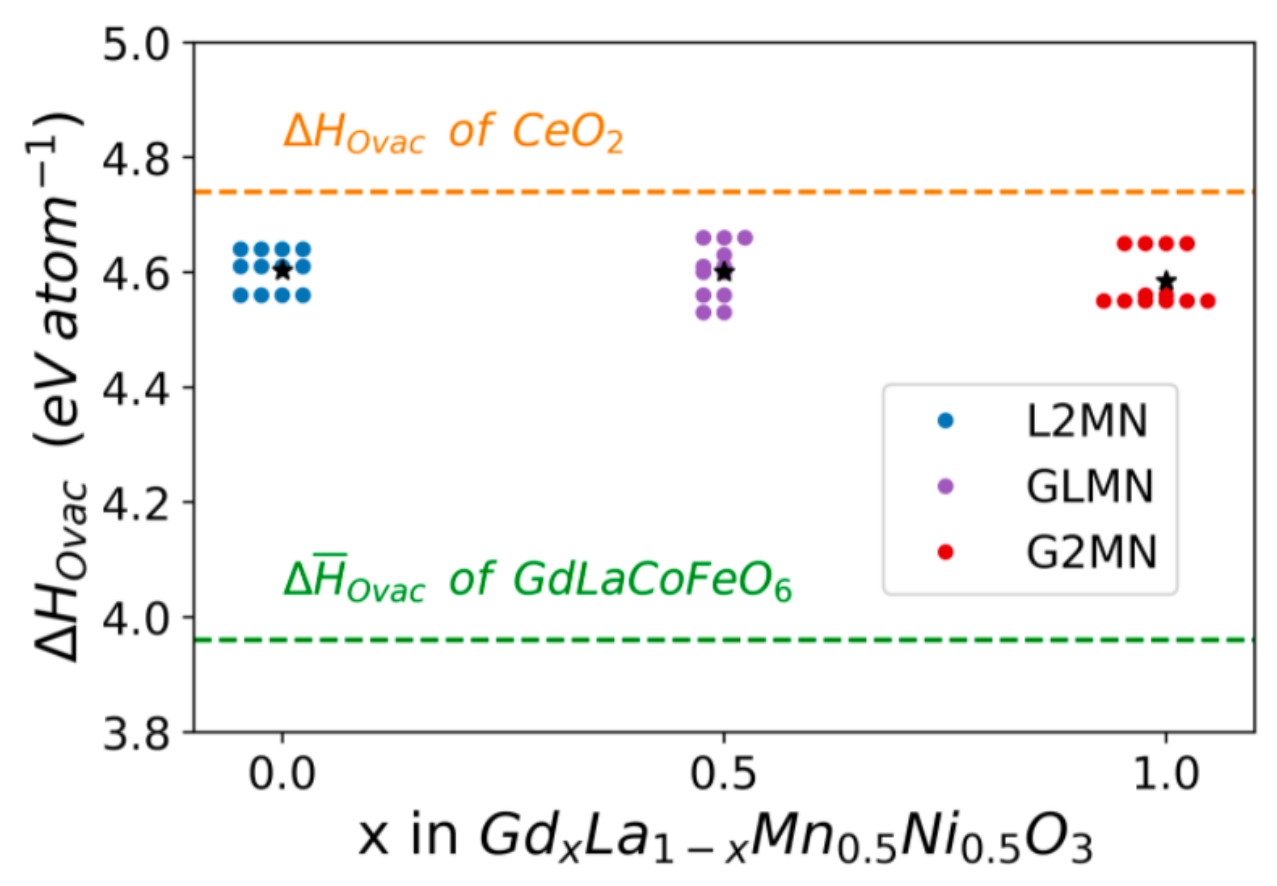


**Figure 3**. Distributions of  $\Delta H_{Ovac}$ s computed with the SCAN functional for L2MN, GLMN and G2MN perovskite oxides, where  $\Delta H_{Ovac}$ s were calculated for all twelve unique oxygen sites in each 20-atom DFT structure.  $\Delta H_{Ovac}$ s that differed by less than 10 meV atom<sup>-1</sup> were deemed equivalent within DFT error, as indicated by the side-by-side circles colored to indicate the host material. Average  $\Delta H_{Ovac}$ s,  $\Delta \overline{H}_{Ovac}$ , are indicated by black stars.  $\Delta \overline{H}_{Ovac} = 4.60$  eV atom<sup>-1</sup> for L2MN,  $\Delta \overline{H}_{Ovac} = 4.60$  eV atom<sup>-1</sup> for GLMN, and  $\Delta \overline{H}_{Ovac} = 4.59$  eV atom<sup>-1</sup> for G2MN, suggesting that these three perovskite compositions will possess similar  $\Delta H_{TR}$ . For comparison, the  $\Delta \overline{H}_{Ovac}$ s of 4.74 and 3.97 eV atom<sup>-1</sup> for the known STCH redox mediators CeO<sub>2</sub> and GdLaCoFeO<sub>6</sub> (GLCF) are also shown, respectively.

The  $\Delta H_{Ovac}$ s of all unique oxygen sites for L2MN, GLMN and G2MN are displayed in **Figure 3**. The average  $\Delta H_{Ovac}$ s,  $\Delta \overline{H}_{Ovac}$ , of L2MN, GLMN and G2MN are 4.60, 4.60, and 4.59 eV atom<sup>-1</sup>, respectively, and are therefore less than the DFT-computed  $\Delta H_{Ovac}$  of CeO<sub>2</sub> ( $\Delta H_{Ovac,CeO_2}$ = 4.74 eV atom<sup>-1</sup>). Also shown is the DFT-computed  $\Delta \overline{H}_{Ovac}$  of the perovskite oxide

redox mediator GdLaCoFeO<sub>6</sub> (GLCF), which was recently demonstrated by Park et al. to be STCH active.<sup>24</sup> The  $\Delta \overline{H}_{Ovac}$ s of L2MN, GLMN and G2MN are much higher than the  $\Delta \overline{H}_{Ovac}$  of GLCF, which suggests that GLMN and L2MN will form lower concentrations of oxygen vacancies than GLCF at  $T_{TR} = 1350$ °C. However, the oxygen vacancies formed by L2MN, GLMN and G2MN should provide greater *thermodynamic driving force* for splitting H<sub>2</sub>O than those of GLCF, as indicated by the larger  $\Delta \overline{H}_{Ovac}$ s of these materials. In the following section(s), we justify the experimental STCH behaviors of the mixed Mn/Ni perovskites, CeO<sub>2</sub> and GLCF using the relative potencies of computationally predicted  $\Delta \overline{H}_{Ovac}$ s.

When oxygen atoms are removed from a metal oxide upon oxygen vacancy formation, the electrons withdrawn from the surrounding metal atoms by the more electronegative oxygens are transferred back to the lattice to occupy electronic states at the Fermi level. All previously reported STCH-active perovskite compositions that reduce via oxygen vacancy formation include at least one redox flexible cation that accepts this electron density. 15,16,22-24 Figures S6a-c of Section V of the SI show the average change in electronic charge,  $\Delta q$ , of nearest-neighbor cations following the removal of a single, charge-neutral oxygen atom from the (a) L2MN, (b) GLMN and (c) G2MN perovskites computed using Bader charge analysis. <sup>39–42</sup> In all compositions, nearest-neighbor Mn<sup>4+</sup> and Ni2+ cations are reduced when oxygen vacancies form. To investigate the extent of these reductions, we compared the magnetic moments  $\mu_B$  of the nearest-neighbor Mn and Ni cations in the bulk and oxygen-defect structures. For reference, the Gd and La f-orbital magnetic moments are the same in the host and defect structures, indicating that these cations remain in the +3 oxidation state following reduction. Figure 4a shows the average change in the magnetic moments of the Mn and Ni nearest-neighbors to the O vacancy of the host and defect structures,  $\Delta \mu_B$ .  $\Delta \mu_B$ of nearest-neighbor Ni cations decreases upon oxygen vacancy formation, consistent with the  $Ni^{2+}$ 

to Ni<sup>+</sup> transition represented by Ni's octahedral field splitting diagram shown in **Figure 4b**. Furthermore,  $\Delta\mu_B$  of nearest-neighbor Mn cations *increases* upon oxygen vacancy formation, consistent with the octahedral field splitting of the Mn<sup>4+</sup> to Mn<sup>3+</sup> transition shown in **Figure 4c**. These results confirm that both Mn<sup>4+</sup> and Ni<sup>2+</sup> are partially reduced following vacancy formation, and suggest that these cations are redox active in L2MN, GLMN and G2MN.

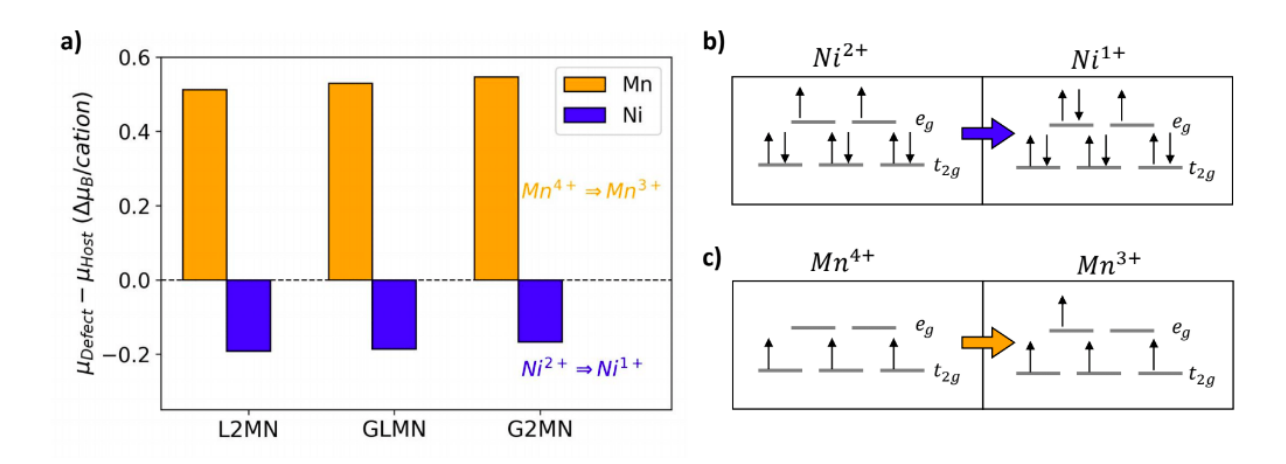


**Figure 4.** a) Differences in d-orbital magnetic moments for Mn and Ni cation nearest-neighbors to the oxygen vacancies of L2MN, GLMN, and G2MN. On average, the magnetic moments  $\mu_B$  increase for Mn and decrease for Ni. b) Octahedral field splitting diagrams for high-spin Ni<sup>2+</sup> and Ni<sup>+</sup> exhibit a decrease in  $\mu_B$  upon reduction, in agreement with the DFT predicted magnetism. c) Octahedral field splitting diagrams for high-spin Mn<sup>4+</sup> and high-spin Mn<sup>3+</sup> exhibit an increase in  $\mu_B$  upon reduction, in agreement with the DFT computed magnetism.

#### D. DFT Computed Oxygen Vacancy Bulk Diffusion Barriers

At STCH thermal reduction conditions, O vacancies form at the redox mediator surface and diffuse into the bulk material. When steam is introduced into the STCH reactor at oxidizing conditions, these vacancies migrate back to the surface, split water and re-oxidize the material. While the vacancies' thermodynamic driving force to reduce water dictates whether water splitting occurs spontaneously, the ease with which O vacancies diffuse through the bulk dictates the rate at which O vacancies migrate to the surface and thus the rate of hydrogen production. Smaller

diffusion barriers correspond with faster redox kinetics, which enables more vacancies to participate in water splitting during a redox cycle and increases total STCH production. DFT has been shown to accurately predict these bulk diffusion barriers. For example, DFT studies of ceria have reported bulk diffusion barriers of between 0.45 eV and 0.60 eV,<sup>43–45</sup> which generally agree with the experimentally determined range of barriers of 0.53 eV to 0.76 eV.<sup>44,46–48</sup>

We computed oxygen vacancy diffusion barriers of 0.78 eV for L2MN, 0.87 eV for GLMN and 0.94 eV for G2MN using the climbing image Nudged Elastic Band (NEB) method<sup>49–53</sup> as implemented in the Vienna Ab-initio Simulation Program, VASP<sup>54–56</sup> (see Computational Details). These DFT computed diffusion barriers are higher than those previously reported for ceria, and trend inversely with the DFT optimized unit cell volumes, where L2MN has the largest volume (230.41 ų) and the smallest transition state barrier. The STCH bulk diffusion kinetics of L2MN, GLMN and G2MN are therefore predicted to be less facile than those of CeO<sub>2</sub>, with G2MN being the most kinetically limited of the three materials. These results suggest that substituting Gd³+ for the larger radius La³+ cation, which causes greater tilting and more asymmetrical distortion of the octahedra as described in Section IB, can inhibit the bulk diffusion of oxygen through the perovskite lattice to the detriment of STCH performance.

#### II. Syntheses of L2MN, GLMN and G2MN, and Measured STCH Activities

A. Synthesis and Confirmation of L2MN, GLMN and G2MN Perovskites

L2MN, GLMN, and G2MN were synthesized using a modified Pechini (citrate gel) method.<sup>57</sup> The metal nitrate salts Gd(NO<sub>3</sub>)<sub>3</sub>·6H<sub>2</sub>O, La(NO<sub>3</sub>)<sub>3</sub>·6H<sub>2</sub>O, Mn(NO<sub>3</sub>)<sub>2</sub>·6H<sub>2</sub>O, and Ni(NO<sub>3</sub>)<sub>3</sub>·6H<sub>2</sub>O (all Sigma Aldrich, > 99% pure) were each dissolved in deionized water, and citric acid was added to each solution in a 2:1 molar ratio of citric acid to total metal cations. The solution was then stirred and heated in a glass beaker at 100°C for 30 minutes, before being heated to 200°C

and held without stirring until a viscous gel formed. The solution was dried overnight at 100°C, and the resulting sample was subsequently ground into a powder and calcined using a two-step process. In the first step, the sample was heated to 850°C for 18 hours in air to form the binary metal oxides. In the second step, the sample was heated to 1500°C for six hours in air to form the perovskite phase. Powder x-ray diffraction (PXRD) was performed on the as-synthesized and postcycled materials with a Bruker D8 Advance diffractometer, using Cu-Kα radiation over the 2θ range between 15° and 100° and a step size of 0.03°. PXRD confirmed the formation of the perovskite phase, as shown in **Figure 5**, and limited phase degradation between the as-synthesized and post-cycled materials, as discussed in Section VI of the SI. As shown in Table 1, lattice parameters and unit cell volumes were characterized by Rietveld refinement using the FullProf crystallographic program.<sup>58</sup> Peak profiles were modelled using a pseudo-Voigt function, and the reported refined parameters include the scale factor, atomic positions, and lattice parameters. Rietveld refinement confirms that the unit cell volumes and lengths of the a and c lattice vectors increase as Gd<sup>3+</sup> is substituted for La<sup>3+</sup>, whereas the length of the b lattice vector decreases, in agreement with or DFT results. PXRD confirms that L2MN, GLMN and G2MN adopt the monoclinic crystal system, which is consistent with previous experimental characterization.<sup>59</sup>

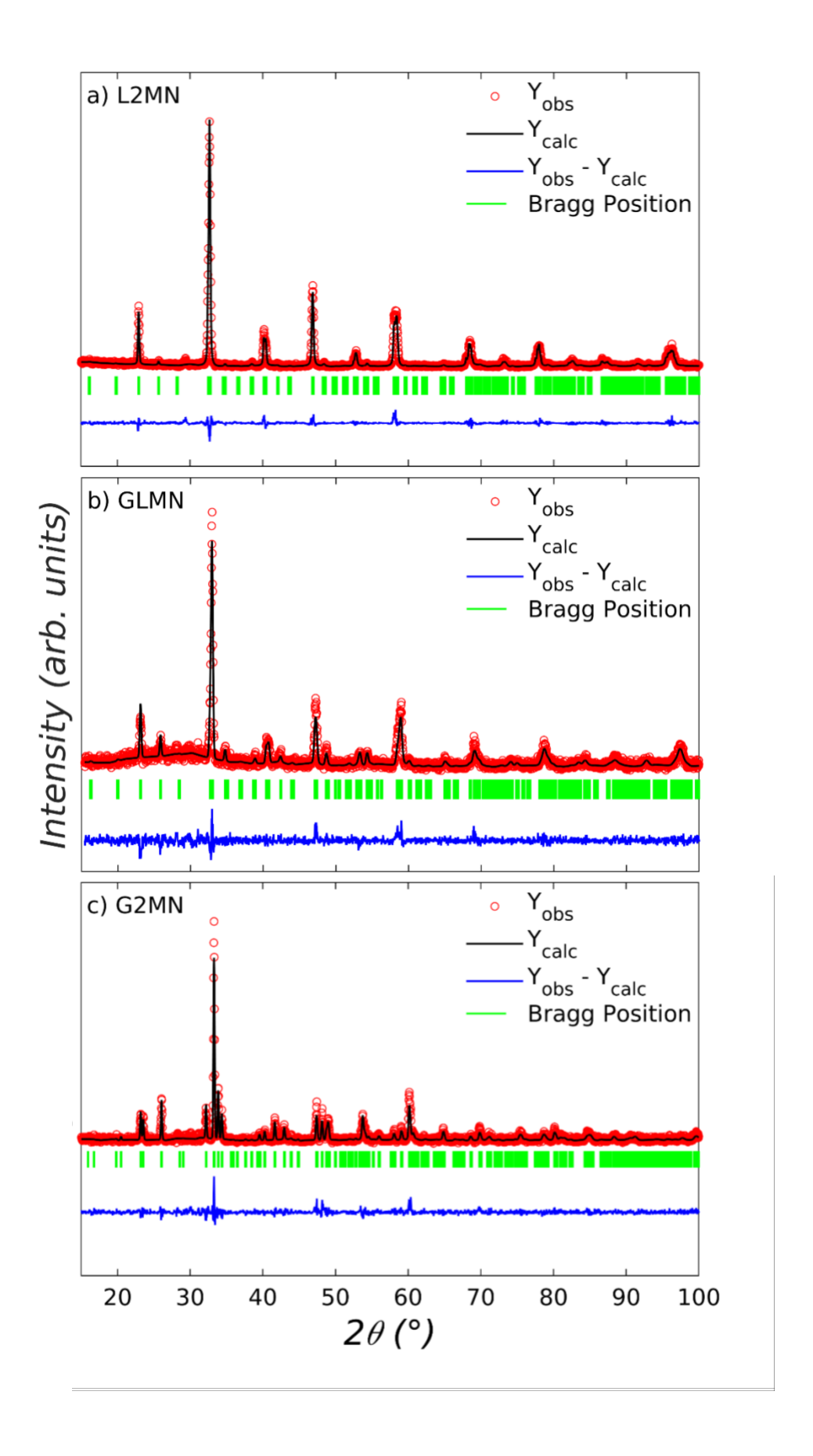


**Figure 5**. Rietveld analysis results for PXRD diffractograms of the a) L2MN, b) GLMN, and c) G2MN perovskite oxides.

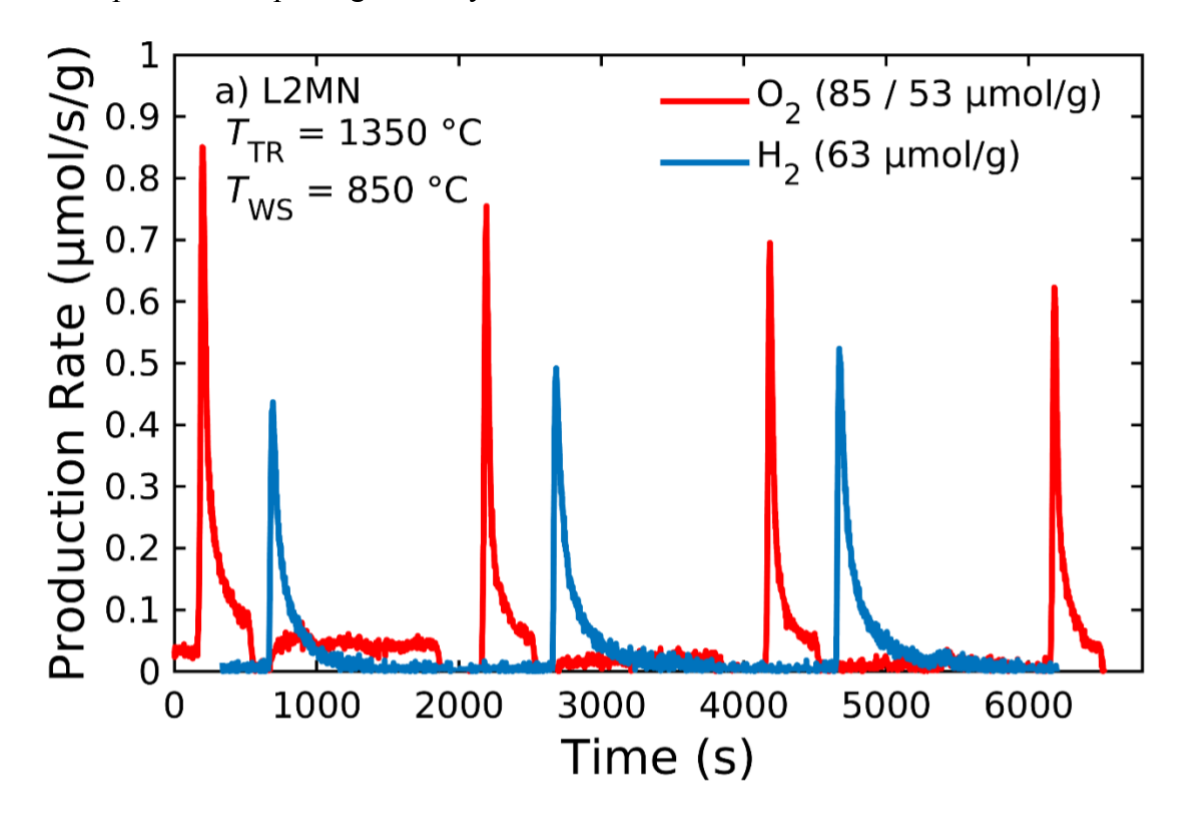
**Table 1.** Rietveld refined structural parameters of L2MN, GLMN, and G2MN.

	L2MN	GLMN	G2MN
a (Å)	5.51393	5.42108	5.29488
b (Å)	5.46382	5.48116	5.56239
c (Å)	7.74594	7.67933	7.55880
α (°)	90.11171	90.04750	89.95772
β (°)	90.07932	89.94762	90.01279
γ (°)	90.02953	89.88694	89.91296
V (Å <sup>3</sup> )	233.362	228.181	222.623
R <sub>p</sub> (%)	15.3	16.3	18.9
Rwp (%)	21.6	20.9	24.1
R <sub>Bragg</sub> (%)	8.85	17.1	17.3
$\chi^2$	1.29	1.20	1.30

### B. The STCH Activities of L2MN, GLMN, and G2MN

STCH activity was tested at Sandia National Laboratories in a stagnation flow reactor (SFR) coupled with a laser-based sample heater and a downstream mass spectrometer. All experiments were conducted at sub ambient pressure (75 torr). Sample aliquots of the ~100 mg powdered materials were placed at the SFR stagnation plane in a shallow, loosely packed bed. A furnace was used to maintain the water-splitting temperature (Tws) at 850°C. Samples were heated from Tws to a reduction temperature TTR = 1350°C by near-infrared laser irradiation at a rate of 10°C s<sup>-1</sup>. Samples were held at TTR for 330 s under a continuous flow of UHP argon (Ar). Following thermal reduction, the laser was turned off and the sample was allowed to cool naturally to Tws (elapsed time ~190 s), after which 40 mol% steam in UHP Ar was flowed over the sample

for a period of 1200 s. The flow rates of oxygen evolved during reduction, and hydrogen produced during oxidation, were measured using a mass spectrometer at a collection rate of ~4 Hz. Representative water splitting cycle data for L2MN and GLMN are shown in **Figure 6**, where both samples were subjected to an initial reduction step from their fully oxidized states, followed by three complete water splitting redox cycles.



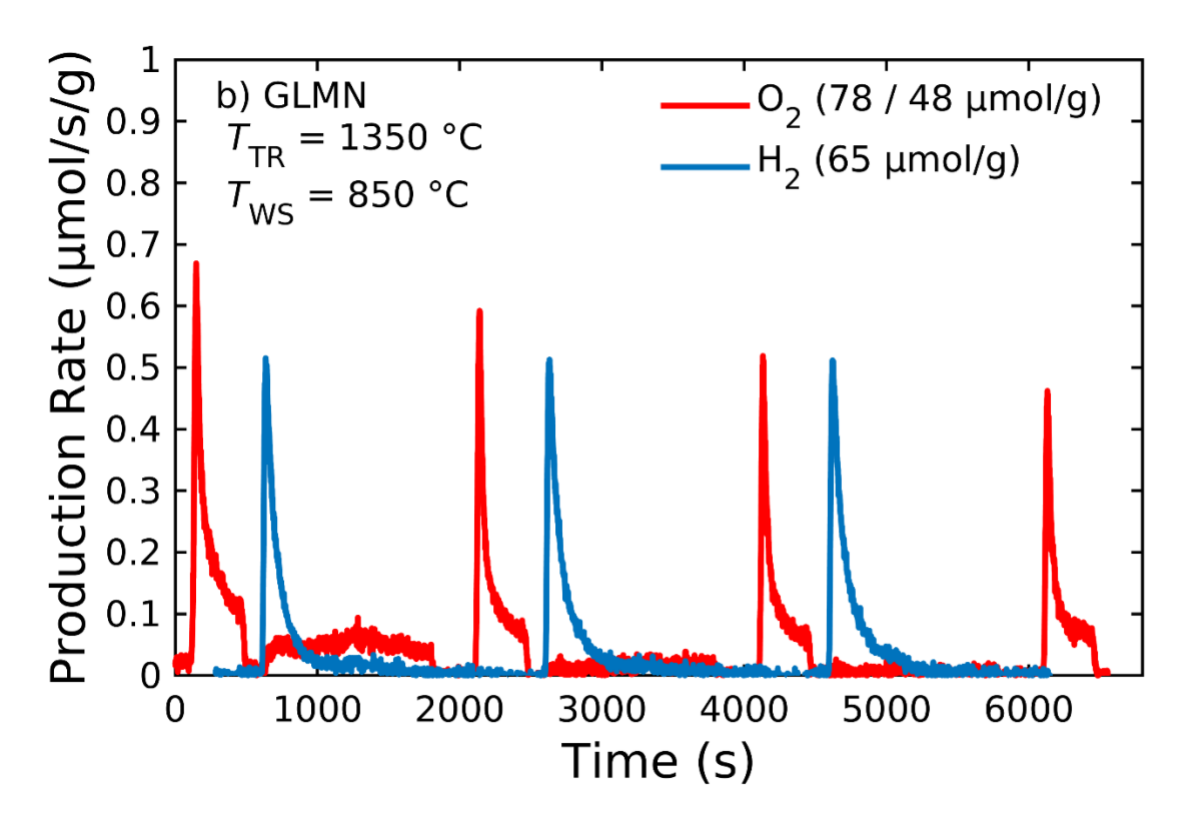


**Figure 6**. Oxygen and hydrogen production rates normalized by sample mass of a) L2MN and b) GLMN.  $T_{TR} = 1350$ °C for 330 s in UHP Ar and  $T_{WS} = 850$ °C for 1200 s in 40 mol% steam in Ar. The legend lists the integrated total for the first oxygen peaks of GLMN and L2MN and the averages of the subsequent oxygen and hydrogen peaks.

L2MN and GLMN exhibited similar hydrogen yields under the conditions tested. L2MN produced 52, 67, and 71  $\mu$ mol g<sup>-1</sup> hydrogen for each consecutive cycle, whereas GLMN produced 64, 65, and 66  $\mu$ mol g<sup>-1</sup> hydrogen for each consecutive cycle. These yields are higher than those observed for CeO<sub>2</sub> (50  $\mu$ mol g<sup>-1</sup>) and lower than those observed for GLCF (67, 90, and 101  $\mu$ mol g<sup>-1</sup> over subsequent cycles)<sup>24</sup> under the same reaction conditions, in qualitative agreement with their computed  $\overline{\Delta H}_{Ovac}$ . In contrast, G2MN produced ~4  $\mu$ mol g<sup>-1</sup> per cycle over two consecutive redox cycles (see SI Section VII), and is therefore considered inactive for STCH. Both L2MN and GLMN exhibited similar peak hydrogen production rates of approximately 0.5  $\mu$ mol g<sup>-1</sup> s<sup>-1</sup>. For both samples, more oxygen evolved during the initial reduction step (85 and 78  $\mu$ mol O<sub>2</sub> g<sup>-1</sup> for L2MN and GLMN, respectively) than in subsequent reduction steps (57, 52, and 49 and 53, 47,

and 44 µmol O<sub>2</sub> g<sup>-1</sup> for L2MN and GLMN, respectively), suggesting that these materials do not return to their fully oxidized state in the 1200 s allotted for water splitting. This behavior has been observed in other water splitting perovskite oxides and is attributed to kinetically-limited reoxidation of these materials<sup>15</sup> as well as to thermodynamic limitations under the milder oxidation conditions of steam relative to oxygen.

### C. STCH Activities under the High Conversion Condition

Additional STCH characterizations of L2MN and GLMN were performed at the "low" steam-to-hydrogen molar ratio of 1333:1 using controlled mixing of hydrogen and steam (a dilute mixture of hydrogen in 40 mol% steam with the H<sub>2</sub>O:H<sub>2</sub> = 1333:1 and Ar balance). These conditions are typically used to evaluate a material's oxidation performance in the presence of the H<sub>2</sub> reaction product, which better represents the operating conditions of industrial reactors. Adding 0.0003 mol% H<sub>2</sub> to 40 mol% steam reduces the equilibrium oxygen fugacity from 1.24·10<sup>-7</sup> atm to 9.28·10<sup>-12</sup> atm under test conditions, which has a profound effect on a material's ability to reoxidize. The system's thermodynamic driving force to split the water molecule and re-populate the redox mediator's lattice oxygen vacancies drops by orders of magnitude under this high conversion condition. However, any material deemed commercially viable will have to maintain water-splitting favorability at H<sub>2</sub>O:H<sub>2</sub> ratios < 10. A water splitting cycle for L2MN, GLMN, and GLCF at the steam-to-hydrogen ratio of 1333:1, and comparison to other known STCH redox mediators, is shown in **Figure 7**.

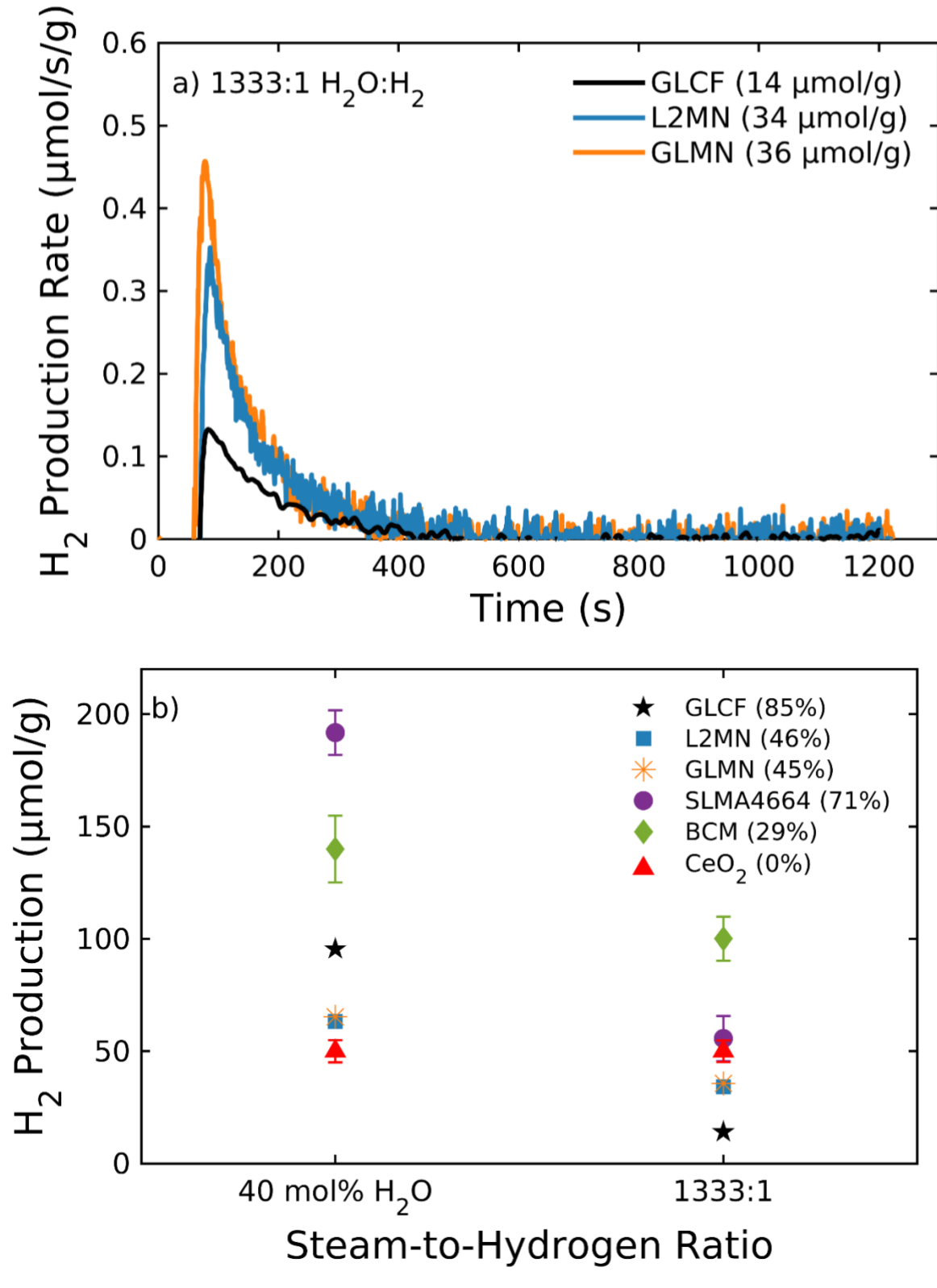


**Figure 7**. a) Mass-normalized H<sub>2</sub> production rate measured under high conversion water splitting conditions of GLCF, L2MN, and GLMN at a 1333:1 steam-to-hydrogen ratio.  $T_{TR} = 1350$ °C for

330 s in UHP Ar and  $T_{WS} = 850^{\circ}\text{C}$  for 1200 s in a mixture of H<sub>2</sub>, H<sub>2</sub>O, and Ar as described in the text. b) Comparison of water splitting activity of GLCF, L2MN, and GLMN to SLMA4664, BCM, and CeO<sub>2</sub> under the same conditions for both 40 mol% steam and high conversion conditions. The legend indicates the percent reduction in water splitting activity from 40 mol% steam to a 1333:1 steam-to-hydrogen ratio.

As discussed above in Section IIB, the water splitting behaviors of L2MN and GLMN are similar under oxidizing conditions where all product H<sub>2</sub> is removed and 40 mol% steam drives reoxidation to the kinetic limit. This suggests that L2MN and GLMN possess similar water splitting thermodynamics (as justified by their similar DFT-computed  $\Delta H_{\text{Ovac}}$  and  $m_e^*$  values) and kinetics at these conditions. Whereas GLMN and L2MN exhibit decreased water-splitting behavior at these conditions relative to GLCF, they exhibit enhanced-water splitting behavior relative to GLCF under high conversion conditions, with production capacities of 36 and 34 µmol g<sup>-1</sup> hydrogen compared to 14 µmol g<sup>-1</sup>. Most known water splitting materials do not produce hydrogen under high conversion conditions due to the low equivalent oxygen partial pressure present during reoxidation (9.28·10<sup>-12</sup> atm for a steam-to-hydrogen ratio of 1333:1). To date, only a few watersplitting materials (including BCM, SLMA and CeO<sub>2</sub>) have been shown to produce hydrogen under these conditions; our results show that GLMN and L2MN successfully maintain ~56% of their hydrogen yields relative to 40 mol% steam conditions. However, GLMN and L2MN exhibit decreasing hydrogen yields with decreasing steam-to-hydrogen ratios, which is similar behavior to that of BCM. This is dissimilar to the behavior of CeO<sub>2</sub>, which exhibits no reduction in hydrogen yield at a steam-to-hydrogen ratio of 285:1.15 We attribute variations in STCH capacities at highconversion conditions to the  $\Delta H_{TR}$  distributions of oxygen vacancies in GLCF, GLMN and L2MN relative to CeO<sub>2</sub>. The  $\overline{\Delta H}_{Ovac}$  of GLMN and L2MN are slightly lower than that of CeO<sub>2</sub> (i.e., < 0.2 eV atom<sup>-1</sup>), and the  $\overline{\Delta H}_{Ovac}$  of GLCF is significantly lower than that of CeO<sub>2</sub> (i.e., > 0.7 eV atom<sup>-1</sup>). While the oxygen vacancies in redox mediators under STCH conditions are not static, i.e.,

vacancies can diffuse through these materials and therefore the  $\Delta H_{\rm Ovac}$  distribution(s) can vary, the  $\overline{\Delta H}_{\rm Ovac}$  of GLMN and L2MN suggests that the oxidation thermodynamics in these materials are less than that of CeO<sub>2</sub> and greater than that of GLCF. Under increasingly higher concentrations of hydrogen present in steam, this should *decrease* STCH production relative to CeO<sub>2</sub> and *increase* STCH production relative to GLCF, at least until an oxygen chemical potential is reached where STCH production ceases for GLCF, L2MN and GLMN.<sup>15</sup>

### **Conclusions**

The DFT-computed electronic properties and distribution(s) of oxygen vacancy enthalpies computed for L2MN, GLMN, and G2MN suggests that these materials will exhibit similar STCH thermodynamics at thermal reduction temperatures  $T_{TR} \leq 1350$ °C. However, DFT computed oxygen vacancy diffusion barriers suggest that the substitution of Gd for La can inhibit redox kinetics. Characterization of water splitting performance over three redox cycles confirmed that GLMN exhibits similar hydrogen production to L2MN (64 µmol g<sup>-1</sup>, 65 µmol g<sup>-1</sup> and 67 µmol g<sup>-1</sup> compared to 52  $\mu$ mol g<sup>-1</sup>, 67  $\mu$ mol g<sup>-1</sup> and 71  $\mu$ mol g<sup>-1</sup>) at  $T_{TR} = 1350$ °C and  $T_{WS} = 850$ °C, but that G2MN is STCH inactive. L2MN and GLMN improve upon the production capacity of CeO<sub>2</sub> at these redox conditions, which is measured to be 50 µmol g<sup>-1</sup>, consistent with the oxygen vacancy enthalpies computed for these materials. At low steam-to-hydrogen ratios (1333:1), GLMN and L2MN exhibit hydrogen production capacities of 36 μmol g<sup>-1</sup> and 34 μmol g<sup>-1</sup> compared to the 50  $\mu$ mol g<sup>-1</sup> production capacity observed in CeO<sub>2</sub> and the 14  $\mu$ mol g<sup>-1</sup>  $\overline{\Delta H}_{Ovac}$ . The high-conversion capacities of GLMN and L2MN lie between those of GLCF and CeO2, which is consistent with the computed  $\overline{\varDelta H}_{Ovac}$ s. The low steam-to-hydrogen ratio conversion observed in GLMN and L2MN is particularly significant, as only certain redox mediators exhibit this behavior, and it substantiates mixed Mn/Ni perovskite oxides as a compelling materials space for STCH

applications. We recommend that the stoichiometric fractions of Mn/Ni in GLMN and L2MN, as well as the identities and stoichiometries of the A-site cations, be further optimized in these materials to maximize STCH production at  $T_{TR} \le 1350$ °C, while attempting to preserve STCH production at low steam-to-hydrogen ratios.

# **Computational Details**

The L2MN, GLMN and G2MN perovskite structures were generated using Structure Prediction and Diagnostic Software (SPuDS),<sup>31</sup> which predicts the magnitude of BO<sub>6</sub> octahedral tilting by minimizing the bond-valence method (BVM)<sup>61</sup> global instability index, *GII*. As demonstrated by Morelock et al., BVM *GII* strongly correlates with the DFT energetics of BO<sub>6</sub> octahedral tilting in experimentally observed ABO<sub>3</sub> perovskite oxide compositions when its *R*<sub>0</sub> parameters are optimized to reproduce DFT relative stabilities.<sup>62</sup> Bare et al. showed that for ternary perovskites the a-b+a- Glazer tilt phase generated by the SPuDS program in the orthorhombic crystal system is the predicted ground state for 95% of experimental and theoretical ABO<sub>3</sub> perovskite oxides.<sup>63</sup> Therefore, in the present work only the a-b+a- Glazer tilt phases of L2MN, GLMN, G2MN and GLCF were generated using SPuDS and optimized using DFT with the SCAN functional, eliminating the computational expense associated with DFT optimization of the six other mixed B-site element Glazer tilts (A<sub>2</sub>BB<sup>3</sup>O<sub>6</sub>) that can be generated by SPuDS.

SCAN calculations were performed using VASP version 5.4.1<sup>54–56</sup> and periodic boundary conditions utilizing projector augmented wave (PAW) pseudopotentials. The electronic wave functions were expanded in a plane wave basis set with an energy cutoff of 600 eV. The Brillouin zones were sampled during geometry optimizations using the Monkhorst-Pack algorithm to automatically generate a  $\Gamma$ -point centered k-point mesh with a grid density of at least 2000/(atoms/unit cell). The specific PAW pseudopotentials used are consistent with pymatgen's

MPScanRelaxSet. Single point magnetic samplings of the L2MN, GLMN and G2MN bulk structures were performed using pymatgen's MagneticStructureEnumerator module. Subsequent  $\Delta H_{\text{Ovac}}$  calculations for defective structures were performed using the same spin-initialization as the magnetically-sampled L2MN, GLMN and G2MN ground states, and calculated in the defect concentration limit  $C_d = 0.0833$  to avoid spurious interactions with periodic images.  $\Delta H_{\text{Ovac}}$  values were computed for all unique oxygen sites in the DFT-optimized L2MN, GLMN and G2MN host structures as determined by pymatgen's SpaceGroupAnalyzer, resulting in a distribution of  $\Delta H_{\text{Ovac}}$  for each perovskite.

The climbing image NEB method<sup>49–53</sup> used herein identifies the transition state by optimizing a set of images interpolated between an initial and final state,<sup>64</sup> with the constraint that images are connected to their neighbors via a spring force. The images therefore cannot shift too far along or outside the initial pathway during optimization, ensuring uniform sampling of the pathway and a realistic transition state upon convergence. Climbing image NEB pushes the highest energy image towards the transition state, which in the present investigation are the transition states corresponding to the oxygen vacancy bulk diffusion barriers of L2MN, GLMN and G2MN. The initial and final images for L2MN, GLMN and G2MN were taken from  $\Delta H_{\text{Ovac}}$  calculations, and are defect structures with two different oxygen vacancy sites that are octahedrally-coordinated by the same B-site cation. All images along the transition state pathways, including transition states, were converged with forces on all atoms of less than 0.05 eV/atom.

## **TOC Figure**

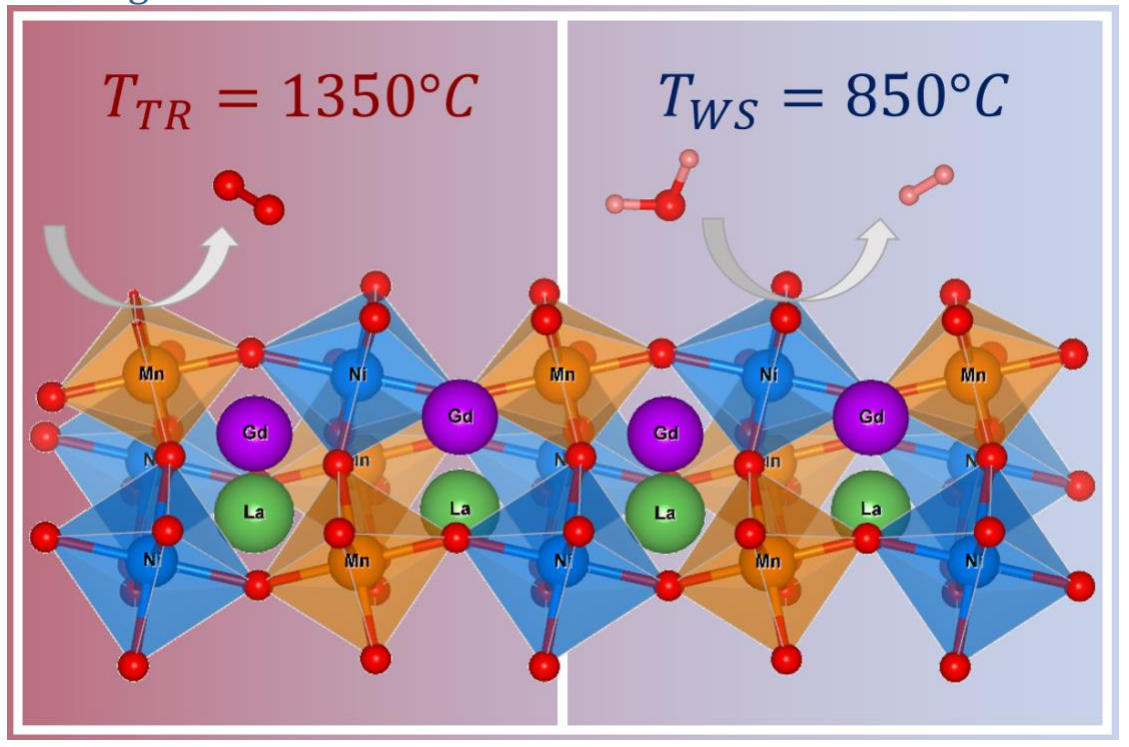


Figure 0. For Table of Contents Only

### **Associated Content**

### **Supplementary Information:**

Brief description of the high-throughput investigation performed by Bare et al. and their reported results for L2MN, GLMN and G2MN --- including DFT-optimized structures, electronic structure properties and oxygen vacancy enthalpies --- computed using the Materials Project's GGA+U framework. A table of L2MN, GLMN and G2MN bulk magnetic moments and corresponding oxidation state assignments. Figures showing the extended pDOSs of L2MN, GLMN and G2MN computed using DFT with the SCAN functional. A figure showing the shift in  $\Delta H_{Ovac}$ s when a different  $\mu_O$  reference potential is used. Figures reporting the differences in cation Bader charge assignment between bulk and defect structures. A figure comparing the as-

synthesized and post-cycled PXRD measurements of L2MN, GLMN, and G2MN. A figure reporting the STCH production of G2MN for 40 mol% steam in Ar.

### **Author Information**

#### **Corresponding Author:**

\*Charles B. Musgrave, charles.musgrave@colorado.edu

#### **Author Contributions:**

‡RM drafted the manuscript and performed the DFT calculations for the bulk and defect L2MN, GLMN and G2MN structures, as well as the reference defect calculations for CeO<sub>2</sub> and GLCF. 
‡JTT synthesized L2MN, GLMN and G2MN, performed the PXRD characterization and Rietveld refinement, and wrote the experimental description. ZB identified L2MN, GLMN and G2MN perovskites as STCH redox mediator candidates from a high-throughput screening investigation, performed the NEB calculations and assisted with DFT property analysis. JAT and AM performed experimental characterization of L2MN, GLMN and G2MN under low and high H<sub>2</sub> conversion. AM supervised experimental characterization. AW supervised the experimental synthesis. CM managed the project, supervised the DFT calculations and assisted with writing of the manuscript. 
‡These authors contributed equally.

#### **Funding Sources:**

This work was supported by the U.S. Department of Energy (DOE), Office of Energy Efficiency and Renewable Energy (EERE), Hydrogen and Fuel Cell Technologies Office (HFTO), and specifically the HydroGEN Advanced Water Splitting Materials Consortium, established as part of the Energy Materials Network under this same office (award DE-EE0008088). CM, ZB and RM also acknowledge support from the National Science Foundation, awards NSF CHEM-1800592 and CBET-2016225. JTT and AW also acknowledge support from the National Science

Foundation Graduate Research Fellowship Program under Grant No. DGE-1650115. Sandia National Laboratories is a multi-mission laboratory managed and operated by National Technology and Engineering Solutions of Sandia LLC, a wholly owned subsidiary of Honeywell International Inc., for the U.S. Department of Energy's National Nuclear Security Administration under contract DE-NA0003525. The views expressed in this article do not necessarily represent the views of the U.S. Department of Energy or the United States Government.

# Acknowledgments

### **Abbreviations**

STCH, solar thermochemical hydrogen; DFT, density functional theory; SCAN, strongly constrained and appropriately normed; GGA+U, generalized gradient approximation with U parameters; L2MN, LaMn<sub>0.5</sub>Ni<sub>0.5</sub>O<sub>3</sub>; GLMN, Gd<sub>0.5</sub>La<sub>0.5</sub>Mn<sub>0.5</sub>Ni<sub>0.5</sub>O<sub>3</sub>; G2MN, GdMn<sub>0.5</sub>Ni<sub>0.5</sub>O<sub>3</sub>; GLCF, GdLaCoFeO<sub>6</sub>; MP, Materials Project database; SPuDS, Structure Prediction and Diagnostic Software; BVM, bond-valence method; DOS, density of states; pDOS, partial density of states; CBM, conduction band minimum; VBM, valence band maximum; NEB, nudged elastic band; VASP, Vienna Ab-initio Simulation Package; PXRD, power X-ray diffraction; SFR, stagnation flow reactor; UHP, ultra-high purity.

### References

- (1) Steinfeld, A. Solar Thermochemical Production of Hydrogen—a Review. *Solar Energy* **2005**, 78 (5), 603–615.
- (2) Centi, G.; Perathoner, S. Towards Solar Fuels from Water and CO2. *ChemSusChem* **2010**, *3* (2), 195–208.
- (3) Muhich, C. L.; Ehrhart, B. D.; Al-Shankiti, I.; Ward, B. J.; Musgrave, C. B.; Weimer, A. W. A Review and Perspective of Efficient Hydrogen Generation via Solar Thermal Water Splitting. *Wiley Interdiscip. Rev. Energy Environ.* **2016**, *5* (3), 261–287.
- (4) Rao, C. N. R.; Dey, S. Solar Thermochemical Splitting of Water to Generate Hydrogen. *Proc. Natl. Acad. Sci. U. S. A.* **2017**, *114* (51), 13385–13393.

- (5) Siegel, N. P.; Miller, J. E.; Ermanoski, I.; Diver, R. B.; Stechel, E. B. Factors Affecting the Efficiency of Solar Driven Metal Oxide Thermochemical Cycles. *Ind. Eng. Chem. Res.* **2013**, *52* (9), 3276–3286.
- (6) Boretti, A. Technology Readiness Level of Solar Thermochemical Splitting Cycles. *ACS Energy Lett.* **2021**, *6* (4), 1170–1174.
- (7) Steinfeld, A. Solar Hydrogen Production via a Two-Step Water-Splitting Thermochemical Cycle Based on Zn/ZnO Redox Reactions. *Int. J. Hydrogen Energy* **2002**, *27* (6), 611–619.
- (8) Abanades, S.; Charvin, P.; Lemont, F.; Flamant, G. Novel Two-Step SnO2/SnO Water-Splitting Cycle for Solar Thermochemical Production of Hydrogen. *Int. J. Hydrogen Energy* **2008**, *33* (21), 6021–6030.
- (9) Nakamura, T. Hydrogen Production from Water Utilizing Solar Heat at High Temperatures. *Solar Energy* **1977**, *19* (5), 467–475.
- (10) Scheffe, J. R.; Weibel, D.; Steinfeld, A. Lanthanum–Strontium–Manganese Perovskites as Redox Materials for Solar Thermochemical Splitting of H2O and CO2. *Energy Fuels* **2013**, 27 (8), 4250–4257.
- (11) Scheffe, J. R.; Li, J.; Weimer, A. W. A Spinel Ferrite/Hercynite Water-Splitting Redox Cycle. *Int. J. Hydrogen Energy* **2010**, *35* (8), 3333–3340.
- (12) Warren, K. J.; Tran, J. T.; Weimer, A. W. A Thermochemical Study of Iron Aluminate-Based Materials: A Preferred Class for Isothermal Water Splitting. *Energy Environ. Sci.* **2022**, *15* (2), 806–821.
- (13) Muhich, C. L.; Evanko, B. W.; Weston, K. C.; Lichty, P.; Liang, X.; Martinek, J.; Musgrave, C. B.; Weimer, A. W. Efficient Generation of H2 by Splitting Water with an Isothermal Redox Cycle. *Science* **2013**, *341* (6145), 540–542.
- (14) Muhich, C. L.; Ehrhart, B. D.; Witte, V. A.; Miller, S. L.; Coker, E. N.; Musgrave, C. B.; Weimer, A. W. Predicting the Solar Thermochemical Water Splitting Ability and Reaction Mechanism of Metal Oxides: A Case Study of the Hercynite Family of Water Splitting Cycles. *Energy Environ. Sci.* **2015**, *8* (12), 3687–3699.
- (15) Barcellos, D. R.; Sanders, M. D.; Tong, J.; McDaniel, A. H.; O'Hayre, R. P. BaCe0.25Mn0.75O3-δ—a Promising Perovskite-Type Oxide for Solar Thermochemical Hydrogen Production. *Energy Environ. Sci.* **2018**, *11* (11), 3256–3265.
- (16) McDaniel, A. H.; Ambrosini, A.; Coker, E. N.; Miller, J. E.; Chueh, W. C.; O'Hayre, R.; Tong, J. Nonstoichiometric Perovskite Oxides for Solar Thermochemical H2 and CO Production. *Energy Procedia* **2014**, *49*, 2009–2018.
- (17) Ezbiri, M.; Takacs, M.; Theiler, D.; Michalsky, R.; Steinfeld, A. Tunable Thermodynamic Activity of La x Sr1-x Mn y Al1-y O3- $\delta$  ( $0 \le x \le 1$ ,  $0 \le y \le 1$ ) Perovskites for Solar Thermochemical Fuel Synthesis. *J. Mater. Chem. A Mater. Energy Sustain.* **2017**, *5* (8), 4172–4182.
- (18) Deml, A. M.; Stevanović, V.; Holder, A. M.; Sanders, M.; O'Hayre, R.; Musgrave, C. B. Tunable Oxygen Vacancy Formation Energetics in the Complex Perovskite Oxide SrxLa1–XMnyAl1–YO3. *Chem. Mater.* **2014**, *26* (22), 6595–6602.
- (19) Nair, M. M.; Abanades, S. Experimental Screening of Perovskite Oxides as Efficient Redox Materials for Solar Thermochemical CO2 Conversion. *Sustainable Energy Fuels* **2018**, *2* (4), 843–854.
- (20) Emery, A. A.; Wolverton, C. High-Throughput DFT Calculations of Formation Energy, Stability and Oxygen Vacancy Formation Energy of ABO3 Perovskites. *Scientific Data* **2017**, *4* (1), 1–10.

- (21) Sai Gautam, G.; Stechel, E. B.; Carter, E. A. Exploring Ca–Ce–M–O (M = 3d Transition Metal) Oxide Perovskites for Solar Thermochemical Applications. *Chem. Mater.* **2020**, *32* (23), 9964–9982.
- (22) Qian, X.; He, J.; Mastronardo, E.; Baldassarri, B.; Wolverton, C.; Haile, S. M. Favorable Redox Thermodynamics of SrTi0.5Mn0.5O3–δ in Solar Thermochemical Water Splitting. *Chem. Mater.* **2020**, *32* (21), 9335–9346.
- (23) Qian, X.; He, J.; Mastronardo, E.; Baldassarri, B.; Yuan, W.; Wolverton, C.; Haile, S. M. Outstanding Properties and Performance of CaTi0.5Mn0.5O3–δ for Solar-Driven Thermochemical Hydrogen Production. *Matter* **2021**, *4* (2), 688–708.
- (24) Park, J. E.; Bare, Z. J. L.; Morelock, R. J.; Rodriguez, M. A.; Ambrosini, A.; Musgrave, C. B.; McDaniel, A. H.; Coker, E. N. Computationally Accelerated Discovery and Experimental Demonstration of Gd0.5La0.5Co0.5Fe0.5O3 for Solar Thermochemical Hydrogen Production. *Front. Energy Res.* **2021**, *9*. https://doi.org/10.3389/fenrg.2021.750600.
- (25) Bare, Z. J. L.; Morelock, R. J.; Musgrave, C. B. A Computational Framework to Accelerate the Discovery of Perovskites for Solar Thermochemical Hydrogen Production: Identification of Gd Perovskite Oxide Redox Mediators. *Adv. Funct. Mater.* **2022**, 2200201.
- (26) Bull, C. L.; McMillan, P. F. Raman Scattering Study and Electrical Properties Characterization of Elpasolite Perovskites Ln2 (BB') O6 (Ln= La, Sm... Gd and B, B'= Ni, Co, Mn). *J. Solid State Chem.* **2004**, *177* (7), 2323–2328.
- (27) Sun, J.; Ruzsinszky, A.; Perdew, J. P. Strongly Constrained and Appropriately Normed Semilocal Density Functional. *Phys. Rev. Lett.* **2015**, *115* (3), 036402.
- (28) Bartel, C. J.; Sutton, C.; Goldsmith, B. R.; Ouyang, R.; Musgrave, C. B.; Ghiringhelli, L. M.; Scheffler, M. New Tolerance Factor to Predict the Stability of Perovskite Oxides and Halides. *Sci Adv* **2019**, *5* (2), eaav0693.
- (29) Bartel, C. J.; Trewartha, A.; Wang, Q.; Dunn, A.; Jain, A.; Ceder, G. A Critical Examination of Compound Stability Predictions from Machine-Learned Formation Energies. *npj Computational Materials* **2020**, *6* (1), 1–11.
- (30) Glazer, A. M. The Classification of Tilted Octahedra in Perovskites. *Acta Crystallogr. B* **1972**, *28* (11), 3384–3392.
- (31) Lufaso, M. W.; Woodward, P. M. Prediction of the Crystal Structures of Perovskites Using the Software Program SPuDS. *Acta Crystallogr. B* **2001**, *57* (Pt 6), 725–738.
- (32) Marianetti, C. A.; Morgan, D.; Ceder, G. First-Principles Investigation of the Cooperative Jahn-Teller Effect for Octahedrally Coordinated Transition-Metal Ions. *Phys. Rev. B Condens. Matter* **2001**, *63* (22), 224304.
- (33) Lany, S. Communication: The Electronic Entropy of Charged Defect Formation and Its Impact on Thermochemical Redox Cycles. *J. Chem. Phys.* **2018**, *148* (7), 071101.
- (34) Naghavi, S. S.; Emery, A. A.; Hansen, H. A.; Zhou, F.; Ozolins, V.; Wolverton, C. Giant Onsite Electronic Entropy Enhances the Performance of Ceria for Water Splitting. *Nat. Commun.* **2017**, *8* (1), 285.
- (35) Jiang, X.; Yin, W.-J. High-Throughput Computational Screening of Oxide Double Perovskites for Optoelectronic and Photocatalysis Applications. *J. Mater. Chem. A Mater. Energy Sustain.* **2021**, *57*, 351–358.
- (36) Barcellos, D. R.; Coury, F. G.; Emery, A.; Sanders, M.; Tong, J.; McDaniel, A.; Wolverton, C.; Kaufman, M.; O'Hayre, R. Phase Identification of the Layered Perovskite Ce XSr2-

- XMnO4 and Application for Solar Thermochemical Water Splitting. *Inorg. Chem.* **2019**, *58* (12), 7705–7714.
- (37) Abanades, S.; Flamant, G. Thermochemical Hydrogen Production from a Two-Step Solar-Driven Water-Splitting Cycle Based on Cerium Oxides. *Solar Energy* **2006**, *80* (12), 1611–1623.
- (38) Chueh, W. C.; Falter, C.; Abbott, M.; Scipio, D.; Furler, P.; Haile, S. M.; Steinfeld, A. High-Flux Solar-Driven Thermochemical Dissociation of CO<sub>2</sub> and H<sub>2</sub>O Using Nonstoichiometric Ceria. *Science* **2010**, *330* (6012), 1797–1801.
- (39) Henkelman, G.; Arnaldsson, A.; Jónsson, H. A Fast and Robust Algorithm for Bader Decomposition of Charge Density. *Comput. Mater. Sci.* **2006**, *36* (3), 354–360.
- (40) Sanville, E.; Kenny, S. D.; Smith, R.; Henkelman, G. Improved Grid-Based Algorithm for Bader Charge Allocation. *J. Comput. Chem.* **2007**, *28* (5), 899–908.
- (41) Tang, W.; Sanville, E.; Henkelman, G. A Grid-Based Bader Analysis Algorithm without Lattice Bias. *J. Phys. Condens. Matter* **2009**, *21* (8), 084204.
- (42) Yu, M.; Trinkle, D. R. Accurate and Efficient Algorithm for Bader Charge Integration. *J. Chem. Phys.* **2011**, *134* (6), 064111.
- (43) Frayret, C.; Villesuzanne, A.; Pouchard, M.; Matar, S. Density Functional Theory Calculations on Microscopic Aspects of Oxygen Diffusion in Ceria-Based Materials. *Int. J. Quantum Chem.* **2005**, *101* (6), 826–839.
- (44) Nolan, M.; Fearon, J. E.; Watson, G. W. Oxygen Vacancy Formation and Migration in Ceria. *Solid State Ionics* **2006**, *177* (35), 3069–3074.
- (45) Nakayama, M.; Ohshima, H.; Nogami, M.; Martin, M. A Concerted Migration Mechanism of Mixed Oxide Ion and Electron Conduction in Reduced Ceria Studied by First-Principles Density Functional Theory. *Phys. Chem. Chem. Phys.* **2012**, *14* (17), 6079–6084.
- (46) Adler, S. B.; Smith, J. W. Effects of Long-Range Forces on Oxygen Transport in Yttria-Doped Ceria: Simulation and Theory. *J. Chem. Soc. Faraday Trans.* **1993**, *89* (16), 3123–3128.
- (47) Chueh, W. C.; Haile, S. M. A Thermochemical Study of Ceria: Exploiting an Old Material for New Modes of Energy Conversion and CO2 Mitigation. *Philosophical Transactions of the Royal Society A: Mathematical, Physical and Engineering Sciences* **2010**, *368* (1923), 3269–3294.
- (48) Dholabhai, P. P.; Adams, J. B.; Crozier, P.; Sharma, R. Oxygen Vacancy Migration in Ceria and Pr-Doped Ceria: A DFT+U Study. *J. Chem. Phys.* **2010**, *132* (9), 094104.
- (49) Jónsson, H.; Mills, G.; Jacobsen, K. W. Nudged Elastic Band Method for Finding Minimum Energy Paths of Transitions. **1998**.
- (50) Henkelman, G.; Jónsson, H. Improved Tangent Estimate in the Nudged Elastic Band Method for Finding Minimum Energy Paths and Saddle Points. *J. Chem. Phys.* **2000**, *113* (22), 9978–9985.
- (51) Henkelman, G.; Uberuaga, B. P.; Jónsson, H. A Climbing Image Nudged Elastic Band Method for Finding Saddle Points and Minimum Energy Paths. *The Journal of Chemical Physics*. 2000, pp 9901–9904. https://doi.org/10.1063/1.1329672.
- (52) Henkelman, G.; Jóhannesson, G.; Jónsson, H. Methods for Finding Saddle Points and Minimum Energy Paths. In *Theoretical Methods in Condensed Phase Chemistry*; Schwartz, S. D., Ed.; Springer Netherlands: Dordrecht, 2002; pp 269–302.
- (53) Sheppard, D.; Terrell, R.; Henkelman, G. Optimization Methods for Finding Minimum Energy Paths. *J. Chem. Phys.* **2008**, *128* (13), 134106.

- (54) Kresse, G.; Hafner, J. Ab Initio Molecular Dynamics for Liquid Metals. *Phys. Rev. B Condens. Matter* **1993**, *47* (1), 558–561.
- (55) Kresse, G.; Furthmüller, J. Efficiency of Ab-Initio Total Energy Calculations for Metals and Semiconductors Using a Plane-Wave Basis Set. *Comput. Mater. Sci.* **1996**, *6* (1), 15–50.
- (56) Kresse, G.; Furthmüller, J. Efficient Iterative Schemes for Ab Initio Total-Energy Calculations Using a Plane-Wave Basis Set. *Phys. Rev. B Condens. Matter* **1996**, *54* (16), 11169–11186.
- (57) Pechini, M. P. Method of Preparing Lead and Alkaline Earth Titanates and Niobates and Coating Method Using the Same to Form a Capacitor. 3330697, July 11, 1967.
- (58) Rodríguez-Carvajal, J. Recent Advances in Magnetic Structure Determination by Neutron Powder Diffraction. *Physica B Condens. Matter* **1993**, *192* (1), 55–69.
- (59) Bull, C. L.; Gleeson, D.; Knight, K. S. Determination of B-Site Ordering and Structural Transformations in the Mixed Transition Metal Perovskites La2CoMnO6 and La2NiMnO6. *J. Phys. Condens. Matter* **2003**, *15*, 4927.
- (60) Scheffe, J. R.; Allendorf, M. D.; Coker, E. N.; Jacobs, B. W.; McDaniel, A. H.; Weimer, A. W. Hydrogen Production via Chemical Looping Redox Cycles Using Atomic Layer Deposition-Synthesized Iron Oxide and Cobalt Ferrites. *Chem. Mater.* **2011**, *23* (8), 2030–2038.
- (61) Brown, I. D. 14 The Bond-Valence Method: An Empirical Approach to Chemical Structure and Bonding. In *Industrial Chemistry Library*; O'Keeffe, M., Navrotsky, A., Eds.; Elsevier, 1981; Vol. 2, pp 1–30.
- (62) Morelock, R. J.; Bare, Z. J. L.; Musgrave, C. B. Bond-Valence Parameterization for the Accurate Description of DFT Energetics. *under Review* **2022**.
- (63) Bare, Z. J. L.; Morelock, R. J.; Musgrave, C. B. Structure and Stability Trends of Computationally Modeled ABO3 Perovskite Oxides. *In progress* **2022**.
- (64) Smidstrup, S.; Pedersen, A.; Stokbro, K.; Jónsson, H. Improved Initial Guess for Minimum Energy Path Calculations. *J. Chem. Phys.* **2014**, *140* (21), 214106.